Review

The Journal of Comparative Neurology
Research in Systems Neuroscience
DOI 10.1002/cne.23432

Medial temporal cortices in *ex vivo* MRI

Jean C. Augustinack [1#], André J.W. van der Kouwe [1], Bruce Fischl [1,2.]

[1] *Athinoula A Martinos Center, Dept. of Radiology, MGH, 149 13th Street, Charlestown MA 02129 USA*
[2] *MIT Computer Science and AI Lab, Cambridge MA 02139 USA*

Correspondence should be addressed:
Jean Augustinack
[1] *Athinoula A Martinos Center*
Massachusetts General Hospital
Bldg. 149, 13th St.
Charlestown, MA 02129
tel: 617 724-0429
fax: 617 726-7422
jean@nmr.mgh.harvard.edu

Keywords: cortical localization, entorhinal cortex, verrucae, perirhinal cortex, perforant pathway

Running title: Medial temporal cortices in MRI

Support for the research was provided in part by the National Center for Research Resources (P41-RR14075, and the NCRR BIRN Morphometric Project BIRN002, U24 RR021382), the National Institute for Biomedical Imaging and Bioengineering (R01EB006758), the National Institute on Aging (AG28521, AG022381, 5R01AG008122-22), the National Center for Alternative Medicine (RC1 AT005728-01), the National Institute for Neurological Disorders and Stroke (R01 NS052585-01, 1R21NS072652-01, 1R01NS070963), and was made possible by the resources provided by Shared Instrumentation Grants 1S10RR023401, 1S10RR019307, and 1S10RR023043. Additional support was provided by The Autism & Dyslexia Project funded by the Ellison Medical Foundation, and by the NIH Blueprint for Neuroscience Research (5U01-MH093765), part of the multi-institutional Human Connectome Project.

Received: Mar 25, 2013; Revised: Jun 27, 2013; Accepted: Jul 10, 2013

ABSTRACT

This review focuses on the *ex vivo* MRI modeling of medial temporal cortices and associated structures, the entorhinal verrucae and the perforant pathway. Typical *in vivo* MRI has limited resolution due to constraints on scan times and does not show laminae in the medial temporal lobe. Recent studies using *ex vivo* MRI have demonstrated lamina in the entorhinal, perirhinal and hippocampal cortices. These studies have enabled probabilistic brain mapping that is based on the *ex vivo* MRI contrast, validated to histology and subsequently mapped onto an *in vivo* spherically warped surface model. Probabilistic maps are applicable to other *in vivo* studies.

The medial temporal lobe houses structures that are critical to normal memory function – the entorhinal cortex and the hippocampus. The circuit that memory formation relies on has been well established. Neural information from multiple modalities converge in the entorhinal cortex and then project to the hippocampus via the perforant pathway (Van Hoesen and Pandya, 1975a; Van Hoesen and Pandya, 1975b; Van Hoesen et al., 1972). When this circuit is damaged surgically (Scoville and Milner, 1957) or damaged due to neurodegenerative pathology such as Alzheimer's disease (Hyman et al., 1984), memory function fails. The two pathological hallmarks in Alzheimer's disease, neurofibrillary tangles and amyloid plaques, manifest differently spatially and temporally in the human brain (Braak and Braak, 1991). The entorhinal and perirhinal cortices exhibit the first neurofibrillary tangles in Alzheimer's disease in their superficial layers. The anterior parahippocampal gyrus includes entorhinal and perirhinal cortices while the posterior parahippocampal gyrus contains posterior parahippocampal cortex (Van Hoesen, 1982). Amyloid plaques appear prior to neurofibrillary tangles primarily in isocortical areas distal to the temporal lobe; however, once neurofibrillary tangles accumulate in the anterior parahippocampal gyrus (entorhinal and perirhinal cortices) and the hippocampus, cognitive impairment is observed (Bennett et al., 2005; Nelson et al., 2009; Savva et al., 2009). Neurofibrillary tangles and neuronal death correlate strongly to cognitive impairment and the density of neurofibrillary tangles and decreased neuronal numbers endure as reliable correlates that predict dementia (Arriagada et al., 1992; Giannakopoulos et al., 2003; Gomez-Isla et al., 1997; Hof et al., 2003). Brain imaging has been invaluable in understanding anatomical and functional properties of these vulnerable cortices in healthy individuals and as well patterns of change with disease (De Toledo-Morrell et al., 2000; Desikan et al., 2009a; Desikan et al., 2009b; Desikan et al., 2010; Desikan et al., 2008; deToledo-Morrell et al., 2004; Dickerson et al., 2009; Dickerson et al., 2011; Insausti et al., 1998a; Insausti et al., 1998b). Even so, brain mapping with specificity and improved accuracy is sought after to improve imaging methods for healthy and disease states.

Over a century ago, Brodmann parcellated the cerebral cortex into cytoarchitectural areas based on structural properties, neuronal size, neuronal packing density, and laminar organization (Brodmann, 1909; Brodmann, 1994). Almost a century after that, the development of magnetic resonance imaging (MRI) (Lauterbur, 1973; Mansfield and Grannell, 1973) facilitated the non-invasive imaging of brain tissue in the living person (Doyle et al., 1981). Structural and functional MRI scans have become staples in assessing brain integrity and function. Functional MRI studies have opened the ability to pose questions about performing tasks in the human brain (Belliveau et al., 1990; Ogawa et al., 1990) and software automates anatomical segmentation for structural MRI (Ashburner and Friston, 1999; Fischl et al., 2002; Fischl et al., 1999a; Fischl et al., 1999b; Fischl et al., 2004b; Jenkinson et al., 2012; Smith et al., 2004). Combining structural and functional brain maps in the same space has enriched neuroanatomical mapping (Amunts and Zilles, 2001; Eickhoff et al., 2006a). Still, more detailed brain mapping is needed especially in clinically vulnerable areas such as the medial temporal cortices. Furthermore, investigating cellular based pathologies in MRI is not possible with *in vivo* imaging. *In vivo* imaging, whether it is structural or functional MRI, permits limited resolution due to constraints on scan time, limited signal-to-noise ratio (SNR) and direct validation in the brain tissue . To tackle these issues, a relatively new model in neuroimaging has emerged that used a tripartite approach (Fischl et al., 2009; Geyer et al., 2011). The tripartite approach utilizes *ex vivo* imaging, histology and *in vivo* probabilistic brain mapping. This review will describe the components of this neuroimaging method and detail some of the findings related to the medial temporal lobe. The review commemorates the life and work of Dr. Gary Van Hoesen, who contributed greatly throughout his career to study the anatomy and connectivity of the hippocampus and parahippocampal gyrus and how these relate to the pathology of Alzheimer's disease. The review focuses primarily on the following structures: the entorhinal cortex, the entorhinal verrucae, the perirhinal cortex, the hippocampal formation, and the perforant pathway and how each has been visualized and modeled with *ex vivo* MRI.

Ex vivo imaging

Utilizing this tripartite approach, *ex vivo* imaging provides an opportunity to make progress where *in vivo* imaging has limitations of scan time, resolution and lacks validation. *Ex vivo* imaging implies scanning postmortem tissue and allows for long scan sessions at high field strengths that yield ultra-high resolution $(100\mu m)^3$ or less and higher SNR images. Equally as important, *ex vivo* imaging facilitates validation of histological properties in high resolution MRI. Notably, this model has no delay between scan and histology where the aging processes can intervene and change properties, which can be a confounding variable in *in vivo* imaging. *Ex vivo* imaging also allows correlation of pathological lesions with MRI intensities (albeit *ex vivo*) (Baltes et al., 2011; Blezer et al., 2007; Cowin et al., 2011; Garbelli et al., 2011; Kangarlu et al., 2007; Nabuurs et al., 2011; Riddle et al., 2011). Although the *ex vivo* model utilizes cross sectional data, it establishes MRI parameters for that particular lesion and helps develop engineering hardware and computational tools that can one day be applicable to *in vivo* studies. *Ex vivo* MRI produces isotropic 3D volumes and permits visualization in several viewing planes unlike histological data that is typically sectioned in coronal plane. The ultimate advantage of *ex vivo* imaging is that it validates the MRI and helps determine what the MRI contrast equals in the histological stained section.

Medial Temporal Lobe Parcellation with Ex vivo MRI

This section details the *ex vivo* MRI contrast in the medial temporal lobe (Augustinack et al., 2013; Augustinack et al., 2005; Fischl et al., 2009) and is the basis for the probabilistic maps described in later sections. Entorhinal, perirhinal and hippocampal cortices will be described. The first figure shows the hippocampus and adjacent parahippocampal cortices in a sagittal slice (Fig. 1A). This plane of cut catches several cortices in the medial temporal lobe at various anterior-posterior levels. The entorhinal cortex (Brodmann's area 28) has a distinctive architecture and corresponds to the anterior parahippocampal gyrus. Surface bumps, known as the verrucae, cover the entorhinal cortex. The entorhinal layer II islands lie directly below the verrucae and are observed in Nissl stained sections and *ex vivo* MRI. The entorhinal layer II islands, which represent the neuron dense clusters in layer II, show up as bright intensities in fast-low-angle-shot (FLASH) images in MRI (Augustinack et al., 2005). The *ex*

vivo FLASH images comprise several types of contrast but T2* dominates (Fischl et al., 2004a). EC Layer III is wide and not as bright as layer II. Lamina dissecans appears as a dark band that segments the supergranular layers from the infragranular layers. EC layer IV appears bright and homogenous. The entorhinal cortex displays its typical architecture with cell clusters in a sagittal slice (Fig. 1A) as well as coronal slices at the level of the anterior hippocampal head (Fig. 1B) and posterior hippocampal head (Fig. 1C). These MRI lamina have been histologically validated in previous studies (Augustinack et al., 2013; Augustinack et al., 2005; Fischl et al., 2009) and corresponding Nissl stained sections are illustrated at the level of the hippocampal head (Fig. 1D) and the hippocampal uncus/body (Fig.1E).

[insert Figure 1 about here]

Perirhinal cortex (Brodmann's area 35) also shows bright intensities in its superficial layers (layer II-III columns in area 35a). Between perirhinal area 35a and 35b, the unique lamina (IIIu of Ding et al 2009) forms an oblique layer that begins in area 35a and ends in area 35b (Augustinack et al., 2013; Ding and Van Hoesen, 2010). Braak and Braak were the first to describe this same oblique layer in transentorhinal cortex (Brodmann's perirhinal area 35a) (Braak and Braak, 1985). Specifically, the large neurons that occupy the superficial portion of entorhinal cortex curve downward to eventually reside in the deeper lamina in isocortex. The superficial layers of area 35b in perirhinal cortex shows a bright homogeneous intensity in *ex vivo* MRI but not organized in columns or islands as do the periallocortical areas (areas 28 and 35a) of the medial temporal lobe. Accordingly, the supragranular layers have a homogeneous bright intensity but the infragranular layers have a dark intensity for that same area (35b). Perirhinal area 35b exhibits a wide dark band in *ex vivo* MRI and it corresponds to the lateral part of the oblique wedge in *ex vivo* MRI (unique IIIu) (Augustinack et al., 2013). The illustrated sagittal plane shows three portions of perirhinal area 35, dorsally at the temporal incisura (between straight white arrows), lateral to the rhinal sulcus (between dotted white arrows) and mostly medial to the collateral sulcus (between curved white arrows) (Fig. 1A). This wide dark band in the middle portion of the lamina is typical of periallocortex/proisocortex in *ex vivo* MRI (Fig. 1A) and in histology (Fig. 1D, 1E) (Augustinack et al., 2013; Ding and Van Hoesen, 2010; Ding et al., 2009). Brodmann's area 35 spills

over the collateral sulcus (laterally) in this case (Fig. 1B, 1D). When the wide dark band ends, it signifies the boundary between proisocortex (perirhinal 35b) and temporal isocortical area 36. In *ex vivo* MRI, temporal isocortical area 36 displays a thin dark line that corresponds to layer IV (Fig. 1A, white carets). Layer IV shows contrast in *ex vivo* MRI likely due to the intracortical myelin in that layer (Augustinack et al., 2013; Eickhoff et al., 2005). Our corresponding histological analyses have confirmed that it is layer IV in our previous study. We have argued that area 36 is temporal isocortex due to the presence of a granular layer IV from our own observations in the human (Augustinack et al., 2013; Van Hoesen et al., 2000) and as illustrated and labeled by Amaral and colleagues in the monkey brain (Amaral et al., 1987). In their report, Amaral and colleagues show a clear layer IV in area 36 (rostral and caudal) in the monkey brain (Amaral et al., 1987). Brodmann noted that, “area 36 – the ectorhinal area – lies, as it’s name implies directly lateral to the rhinal sulcus and represents the first area of neopallium adjacent to the archipallium.” Moreover, area 36 has six distinct laminae and distinct granularity, both of which defines the isocortical tissue type (Brodmann, 1909; Filimonov, 1949; Gloor, 1997; Mesulam and Mufson, 1982; Pandya and Yeterian, 1985; Sanides, 1969; Stephan, 1975; Van Hoesen et al., 2000). In the human brain, we have observed that it is perirhinal area 35b that displays a poor layer IV (i.e. incipient) but that area 36 has a fairly well-developed layer IV. It is important to note that, in the human brain, perirhinal area 35 represents a bipartite cortex that is periallocortex (35a) *and* proisocortex (35b) while area 36 is isocortex (Augustinack et al., 2013; Van Hoesen et al., 2000). The modularity and distinctive structures of entorhinal and perirhinal cortices allow for straightforward parcellation in *ex vivo* MRI. In fact, we routinely observed architectonic field boundaries in *ex vivo* MRI in this region before histological analyses were carried out.

The subicular cortices are located inferior to the hippocampus (Fig. 1). In the illustrated slice, the presubiculum extends the entire length of the hippocampal head and body between the asterisks (Fig 1A). The presubiculum routinely displays presubicular clouds (grouped neurons in the presubiculum that the perforant pathway projects through (Van Hoesen and Pandya, 1975b) that appear bright in *ex vivo* MRI, while the parasubiculum reveals a homogeneous layer superficially (Fig. 1C). Several lamina

in the hippocampus are also discernible: the alveus, the molecular layer of the hippocampus (stratum lacunosum of Lorente de Nó (Lorente de No, 1934)), and the pyramidal cell layer. The alveus and molecular layer appear consistently dark *in ex vivo* MRI, while the pyramidal layer shows a bright appearance. With enough averages and a brain with good contrast, the mossy fiber layer (stratum lucidum of Lorente de Nó) is observed as a dark band inferior to the lighter pyramidal layer (Fig. 1C). The granule layer of the dentate gyrus conveys a bright intensity in *ex vivo* MRI. Typically, the granule cell layer is as bright as the entorhinal islands. Our MRI findings in medial temporal lobe suggest that bright intensities in *ex vivo* MRI represent densely packed neuronal layers (i.e. entorhinal islands, perirhinal columns and granule cells of dentate gyrus) and that dark intensities represent myelin-rich lamina or neuronal-sparse areas (i.e. the inter-islands in area 28) in T2* weighted FLASH images.

Probabilistic Mapping

The ability to visualize populations of neurons and density of myelin with high resolution MRI has had an extensive impact and reshaped the field of brain mapping (Augustinack et al., 2005; Barbier et al., 2002; Bridge and Clare, 2006; Clark et al., 1992; Duyn et al., 2007; Eickhoff et al., 2005; Fatterpekar et al., 2002; Post, 2008; Walters et al., 2003). The capability to correlate MRI with histology has provided validated maps based on cytoarchitecture, myeloarchitecture, multi-receptor architecture and pathoarchitecture and adding depth to neuroanatomical imaging (Amunts et al., 2005; Amunts et al., 2007; Amunts and Zilles, 2001; Augustinack et al., 2012b; Augustinack et al., 2013; Eickhoff et al., 2005; Eickhoff et al., 2006b; Fatterpekar et al., 2002; Howe et al., 2010; Rademacher et al., 2001; Scheperjans et al., 2008a; Scheperjans et al., 2008b; Zilles and Amunts, 2009). Based on the *ex vivo* MRI contrast described in the previous sections, the boundaries of entorhinal and perirhinal cortices (Brodmann's area 28 and 35, respectively) were determined on the high-resolution images (Augustinack et al., 2013; Fischl et al., 2009). High resolution *ex vivo* data were manually labeled using anatomically defined protocols to create labels of entorhinal and perirhinal cortices. These structures were labeled across several cases at $(120\ \mu m)^3$ and each label was registered onto its respective hemisphere volume $(1\ mm)^3$ using Register (Register (MNI toolkit, Montreal, Canada,

http://www.bic.mni.mcgill.ca). Subsequently, the labels of many cases were transformed onto an average surface template and that predicts the cortical localization. This creates the histologically-validated entorhinal (Fig. 2 A) and perirhinal (Fig. 2 C) probability maps based on spherical warping. The entorhinal label extends from the primary olfactory cortex to midway on the parahippocampal gyrus (Fig. 2 A). Throughout its course, entorhinal cortex remains on the crown of the parahippocampal gyrus. The perirhinal label extends from the anterior temporal incisura area to midway on the parahippocampal gyrus (Fig. 1A, 2 B). The depth of the collateral sulcus conceals the middle portion of perirhinal label in the partially inflated brain. The sulci in the medial temporal lobe complicate the topography of perirhinal cortex. Perirhinal cortex (Brodmann's area 35) involves two different sulci, the collateral and the rhinal sulcus and extends slightly into the temporal incisura. For the majority of its territory, perirhinal cortex resides on the lateral side of the rhinal sulcus but at middle levels, it resides on the medial side of the collateral sulcus. At the posterior levels, perirhinal label appears on the crown of parahippocampal gyrus just briefly, before it ends (Fig 2C, 2D). With the accomplishment of being able to visualize the lamina of the medial temporal cortices, it has become possible to parcellate the entorhinal and perirhinal cortices in *ex vivo* MRI, to establish areal boundaries, and to create histologically validated labels for application to future *in vivo* studies. The labels generated can be applied to structural and functional MRI *in vivo* brain mapping. For example, application to larger cohort studies in aging and disease studies shows differences in cortical thickness among diagnostic groups (Augustinack et al., 2013; Fischl et al., 2009). In sum*, ex vivo* imaging provides the ability to improve brain mapping by linking the 'ground truth' histology with MRI based surface models that apply to *in vivo* imaging models.

[insert Figure 2 about here]

Sulcal complexity in the medial temporal lobe

The rhinal sulcus varies considerably in the human brain (Figure 3) (Hanke, 1997; Insausti et al., 1998b; Ono, 1990 ; Van Hoesen et al., 2000). The rhinal sulcus ranges from a significant one (Fig. 3A) to a more subtle one (Fig. 3B and C) to a shallow groove (Fig. 3D). Zuckerkandel noted that 86% of

brains in his collection did not have a rhinal sulcus (Zuckerkandl, 1887). The Victorian comparative anatomist Richard Owen coined the term 'ecto-rhinal' or 'rhinal sulcus' to denote the border between olfactory cortex (the olfactory peduncle) and frontal cortex (lateral to the peduncle) in the human brain (Owen, 1868). Thus, the term 'rhinal sulcus' was fixed to the border between rhinencephalon and other cortex. Owen used the terms ecto-rhinal and rhinal interchangeably and later William Turner shortened the term ecto-rhinal sulcus to rhinal sulcus (Turner, 1890). Several turn of the century neuroanatomists neglected to label the rhinal and collateral sulci in primates (Ariens-Kappers et al., 1967; Broca, 1878; Brodmann, 1909; Retzius, 1896; Turner, 1890), while others mislabeled the sulci (Connolly, 1950; Krieg, 1973; Netter, 1989; Smith, 1903). Both trends were likely due to the sulci variability and nomenclature uncertainty. Monkeys (Fig. 4A) and great apes have a long rhinal sulcus that extends from the anterior medial part of the temporal lobe to the posterior levels of the parahippocampal gyrus. The sulcal topography in monkeys differs from great apes in that monkeys do not have a collateral sulcus, whereas apes and humans do (Fig 3, 4A, 4B). The complication that a cortical area (perirhinal cortex, area 35) weaves through several sulci and that many human brains do not have a rhinal sulcus underscores an important point that cytoarchitecture based analyses produce more accurate architectonic mapping than sulcal based ones (Amunts et al., 2005; Augustinack et al., 2013). Probabilistic mapping validated with histological architecture provides a dependable method to map regardless of sulcus presence, absence or particular depth.

[insert Figure 3 about here]

Surface geometry of the entorhinal cortex

High-resolution imaging with *ex vivo* samples has advanced the modeling of small structures. In the human brain, the entorhinal cortex displays small bumps on its surface (Klingler, 1948; Retzius, 1896). The surface bumps are termed entorhinal verrucae (Fig. 4B, 4C) and clusters of layer II entorhinal islands lie directly beneath them. Thus, the verrucae correspond with the entorhinal islands, one verruca for each entorhinal island. Notably the monkey entorhinal cortex does not show verrucae (Fig. 4A) and this suggests that the verrucae are a human entorhinal feature. In the monkey entorhinal

cortex, layer II organizes into islands but to a lesser degree than the human entorhinal cortex. The entorhinal layer II in the monkey brain tends to elongate and is less circular than observed in the human entorhinal cortex. In humans, the majority of the entorhinal cortex displays clusters of entorhinal islands. It is unknown whether the absence of verrucae in monkeys is due to neuronal size or island shape (i.e. elongated island) but further comparative studies about the verrucae would establish definitive evidence. In the human brain, it is thought that the large neurons that make up layer II cause the bulging onto the surface but synapses may also play a role. In Alzheimer's disease, the entorhinal verrucae disappear (Augustinack et al., 2012b; Solodkin and Van Hoesen, 1996; Van Hoesen et al., 2000; Van Hoesen and Solodkin, 1993). Simic and colleagues documented that entorhinal verrucae decrease in surface area during aging yet this brain collection revealed a laterality relationship (more verrucae on the left) and an increase in number of verrucae with age (Simic et al., 2005). Volumetric measures in the medial temporal lobe in patients have shown that atrophy in the right entorhinal cortex predicts the conversion from healthy to mild cognitive impairment (De Toledo-Morrell et al., 2000). Although these two studies were assessed in different conditions (*in vivo* versus *ex vivo*), it may be postulated that verrucae represent a structural marker of cognitive resilience. Further studies are necessary to pinpoint the factors contributing to cognitive resilience.

Assaying entorhinal verrucae quantitatively and qualitatively

High resolution *ex vivo* imaging gives us a closer look at the entorhinal surface and provides a model for quantitative measurement of individual verrucae. From *ex vivo* MRI volumes, a 3D isosurface is generated with Freeview (FreeSurfer, http://surfer.nmr.mgh.harvard.edu). The gross morphometry (or photographic image) (Fig. 4B) validates the verrucae isosurface reconstruction (Fig. 4C) and the isosurface represents a detailed three dimensional model of the surface. The isosurface allows for measurement of individual verruca (Fig. 4C). Our verrucae metric algorithm uses an optimal least squares fitting plane at the base of the isosurface and then measures verruca height, width, surface area and calculates verruca volume (Fig. 5A) (Augustinack et al., 2012b). Verrucae qualitative ratings correlate with verrucae height and volume (Augustinack et al., 2012b). The dimensions of a large

verruca range from 0.20 - 0.25 mm in height and almost 2 mm for width. Medium-sized verrucae extend to approximately 0.15 mm - 0.19mm. Observed differences in these verrucae measurements reflect a pathologic change in layer II and in diagnosis (Augustinack et al., 2012b). Differences in verrucae size, especially verrucae height, indicate mild Alzheimer's cases from control brains. Furthermore, verruca size negatively correlates with disease severity based on Braak and Braak staging (Augustinack et al., 2012b; Braak and Braak, 1991). A surface measurement below 0.10 mm denotes flat cortex. This flat cortex could be an Alzheimer's case or other types of cortex that do not exhibit verrucae (motor, prefrontal, occipital, parietal or cingulate cortices) (Augustinack et al., 2012b). Finally, curvature measures (mean and Gaussian) in FreeSurfer correlate with verrucae height and volume as well (Augustinack et al., 2012a).

[insert Figure 4 about here]

[insert Figure 5 about here]

While existing *in vivo* technology is not able to resolve verrucae, investigating the entorhinal verrucae *ex vivo* allows us to better define this unique structure, and examine individual differences in human populations. Since technology continually progresses, it is tempting to predict the required resolution to detect verrucae *in vivo*. Based on downsampling results from control *ex vivo* cases, it is estimated that 300 μm isotropic resolution is needed to resolve entorhinal verrucae. When 100 μm MRI data was downsampled to 300 μm, the verrucae were still visible, but not at 500 μm. Given that this is close to current high-resolution *in vivo* imaging standards, imaging verrucae *in vivo* may soon be feasible with further technical developments.

The perforant pathway

Diffusion imaging allows the estimation of brain fiber orientation by measuring water diffusion. In diffusion imaging, fiber pathways are inferred based on the amount of anisotropy in the measured diffusion (along a fiber in a certain orientation) (Basser, 1994; Basser et al., 1994). Because white matter is organized in axonal bundles, the diffusional anisotropy of water is higher than gray matter,

which has neurons mixed with fibers. This variation in diffusional anisotropy is a useful contrast for measuring anatomical properties. Alveus, temporal stem, angular bundle and perforant pathway all have high fractional anisotropy (bright white signal) (Fig. 6A). Diffusion voxels contain directionality and that allows visualization of fiber pathways with fiber tracking software (http://www.trackvis.org/). *Ex vivo* tractography streamlines illustrate the perforant pathway (Fig. 6B). The vertical green fibers represent the perforant pathway in this deterministic paradigm but have also been demonstrated with probabilistic tractography and fractional anisotropy (Augustinack et al., 2010; Shepherd et al., 2007). This tractography volume has been edited in order to show and highlight the perforant pathway without other fibers obstructing the view. The tractography image is a 3D volume so fibers on the right side of the image actually reside in an anterior slice (Fig. 6B) and as a result, the image (Fig. 6B) appears larger than (Fig 6A and 6C). The perforant fibers appear short, appropriately so, because these fibers terminate at the outer two-thirds of the molecular layer of the dentate gyrus and the entire molecular layer of the hippocampus (stratum lacunosum), which is a short distance from the sulcus (Fig. 6B, 6C). The perforant pathway is the only known pathway that crosses a sulcus to reach its destination synapse. A few imaging studies have also examined the perforant pathway *in vivo* (Yassa et al., 2010; Zeineh et al., 2012). These studies require acquisitions with isotropic voxels to assess the small features of the perforant pathway.

[insert Figure 6 about here]

Technical Considerations

Ex vivo MRI acquisition and surface reconstruction

Probability maps require scanning at two resolutions, a lower resolution (1mm x 1mm x 1mm) at lower field (1.5T or 3T) for surface reconstruction, and a higher resolution (100μm x 100μm x 100μm) at 7.0 Tesla for direct visualization of microscopic features of the anatomy. MRI volumes of the entire hemisphere (i.e. lower resolution) are acquired with a routine *in vivo* morphometry scan and generate surface models based on spherical warping for each case (FreeSurfer, http://surfer.nmr.mgh.harvard.edu) (Fischl et al., 1999a; Fischl et al., 1999b). Subsequently, smaller

blocks of the medial temporal lobes (i.e. higher resolution) scanned at 7T (Siemens, Erlangen, Germany) using a four-turn solenoid coil and a 3D spoiled gradient echo sequence generate the resolution that allows for cytoarchitectural detection. A single echo, isotropic FLASH sequence is used to acquire volumes with 100 μm isotropic resolution. Scanning with small coils at higher field strength yields a significant increase in SNR that can be used to achieve higher resolution.

Registration

Ex vivo studies require an extra step to register the two modalities together. Registration is needed for not only *ex vivo-in vivo* MRI correlations (Register, MNI toolkit, Montreal, QC CA) but also *ex vivo*-histology correlation (in house software, HistoRegister) (Reuter et al., 2012; Sand and Teller, 2008; Wachinger, 2010). Probabilistic mapping depends on good registration. At times, registration can challenge the most patient and spatially competent of us due to poor contrast and oblique- and difficult-to-recognize planes and physical deformations of the tissue in the scanning tube. The integrity of human tissue varies significantly (compared to animal studies) due to many and possibly unknown factors.

Conclusion

Over the last several decades, the term brain mapping has had different meanings. Brain mapping has progressed from purely anatomical and cytoarchitectural maps, to connectivity tracing in animal models and recently to probabilistic mapping in a common structural and functional MRI space. Cumulative advances in brain mapping coupled with technological innovation will improve our knowledge of the medial temporal lobe as well as other regions in the human brain. Given the fact that *ex vivo* MRI now visualizes neuronal dense lamina and cell clusters, it may provide insight into what we will observe in future *in vivo* MRI.

FIGURE LEGENDS

Figure 1 – *Ex vivo* MRI of medial temporal lobe structures at (120 μm)^3 . (A) Sagittal plane through the parahippocampal gyrus and hippocampus shows lamina and neuroanatomical features. The pes of the hippocampus are shown posterior to the amygdala. The hippocampus and dentate gyrus are intertwined at posterior hippocampal head. Molecular layer, pyramidal layer and alveus are evident in (B) and (C). The presubiculum displays light and dark intensities and extends between the asterisks. Entorhinal layer II demarcated with light and dark intensities while layers III and IV are more homogeneous. Perirhinal cortex surrounds entorhinal cortex anteriorly (between dotted arrows) and posteriorly (between curved arrows). Note, perirhinal cortex is also observed dorsally (between straight arrows). Temporal isocortical area 36, denoted with a dark intensity in layer IV (white ^) is lateral to perirhinal area 35. (B) and (C) represent coronal planes of cut through hippocampal head and adjacent cortex. On medial bank of collateral sulcus, perirhinal cortex shows the oblique wedge with light intensity superficially and dark intensity in inferior lamina. Perirhinal cortex ends near the fundus in (B, D) and on the crown of parahippocampal gyrus as collateral sulcus ends in (C) and (E). (D) and (E) show the equivalent slices stained for Nissl substance. In this case, the collateral sulcus ends immediately before the level of (C) for MRI and (E) for Nissl section and remains as a very subtle indentation. Since the collateral sulcus has ended in (C), the sulcus that is lateral to the collateral sulcus remnant is the occipitotemporal sulcus. Double asterisk (**) = boundary between area 28 and area 35. The black caret (^) represents the boundary between area 35 and area 36. Marked x's in hippocampal head (D) denote that CA1 is transitioning to CA2 in this section but not fully realized. alv = alveus, Am = amygdala, BA = Brodmann's area, CA = cornu ammonis, CP = choroid plexus, EC = entorhinal cortex, DG = dentate gyrus, HP = hippocampus, iso = isocortex, , mf = mossy fiber layer, ml= molecular layer, OTS = occipitotemporal sulcus, PC = perirhinal cortex, pyr = pyramidal layer, TP = temporal pole, ParaS = parasubiculum, PreS = presubiculum, x = transition between CA1 and CA2. Magnification bar = 1 cm in (A) and 0.5 cm in (B, C, D, E).

Figure 2 – Average probability maps for entorhinal (A) and perirhinal (B) cortices in left hemisphere (n = 9; n = 8, respectively) and right hemispheres (n = 7, n = 8, respectively). The red represents the region of highest probability and 100% overlap of cases. In all panels, the spherical models were partially inflated and labels are displayed on the pial surface. Note the entorhinal label (Brodmann's area 28) on the crown of the parahippocampal gyrus and the perirhinal label (Brodmann's area 35) primarily in the sulcal depths and partially on the crown of the gyrus. Each label tapers posteriorly until it ends.

Figure 3 – Variability of the rhinal and collateral sulciin the human brain. Rhinal sulcus is highly variable with definite sulcus in (A), shorter and more subtle in (B and C) and a groove in (D). CS = collateral sulcus, OTS = occipitotemporal sulcus, RG = rhinal groove, RS = rhinal sulcus. The collateral and occipitotemporal sulci are variable as well but they maintain a more traditional depth in these cases. Magnification bar = 1 cm.

Figure 4 – Entorhinal cortex in macaque monkey gross photograph (A), human gross photograph (B) and human isosurface reconstructed from MRI volume at (120 um) ^{3} (C). Note the verrucae in (B) and (C) and the lack of verrucae in (A). Black carets (^ ^) point to individual verruca. CS = collateral sulcus, EC = entorhinal cortex, HF = hippocampal fissure,, RS = rhinal sulcus.

Figure 5 – Schematic drawing of entorhinal verrucae and MRI slice at $(100\mu m)^3$. The schemata details verrucae measurements obtained from our algorithm in (A). Entorhinal verrucae shown in MRI slice (zoomed to two verrucae) in (B). Magnification bar in (B) = 0.5cm.

Figure 6 – *Ex vivo* diffusion tensor imaging in the medial temporal lobe at $(300\mu m)^3$. Fractional anisotropy in (A), tractography streamlines in (B) and Gallyas myelin stained tissue in (C). Note the vertical oriented fibers in both (B) and (C). Curved arrows in (B) and (C) point to the perforant pathway (pp). (B) appears slightly larger than the other panels because (B) is a 3D image and some of the streamlines (i.e. green, yellow, orange tracks) actually reside anterior to the slice displayed. Thin

straight arrow in (C) demarcates the hippocampal efferents projecting back to the angular bundle. Magnification bar = 0.5 cm.

Other acknowledgments. The authors would like to thank those who generously donated the brain and made this research possible. We thank Matthew Frosch for brain procurement and we acknowledge and thank Allison Stevens Player, Sita Kakunoori, Kristen Huber, Karl Helmer, and Ruopeng Wang for excellent technical assistance.

Role of authors. All authors had full access to all the data in the study and take responsibility for the integrity of the data and the accuracy of the data analysis. Study concept and design: JCA, AVDK, BF. Acquisition of data: JCA, AVDK. Analysis and interpretation of data: JCA, BF. Drafting of the manuscript: JCA. Critical revision of the manuscript for important intellectual content: JCA, AVDK, BF. Statistical analysis: JCA. Obtained funding: JCA, BF. Technical support: AVDK. Study supervision: JCA, BF.

Conflict of Interest Statement. Bruce Fischl would like to disclose he is part owner of a company CorticoMetrics, LLC; the other two authors have nothing to disclose.

Literature Cited

Amaral DG, Insausti R, Cowan WM. 1987. The entorhinal cortex of the monkey: I. Cytoarchitectonic organization. The Journal of comparative neurology 264(3):326-355.

Amunts K, Kedo O, Kindler M, Pieperhoff P, Mohlberg H, Shah NJ, Habel U, Schneider F, Zilles K. 2005. Cytoarchitectonic mapping of the human amygdala, hippocampal region and entorhinal cortex: intersubject variability and probability maps. Anat Embryol (Berl) 210(5-6):343-352.

Amunts K, Schleicher A, Zilles K. 2007. Cytoarchitecture of the cerebral cortex--more than localization. Neuroimage 37(4):1061-1065; discussion 1066-1068.

Amunts K, Zilles K. 2001. Advances in cytoarchitectonic mapping of the human cerebral cortex. Neuroimaging Clin N Am 11(2):151-169, vii.

Ariens-Kappers CU, Huber GC, Crosby EC. 1967. The comparative anatomy of the nervious system of vertebrates, including man. New York: Hafner Publishing Company.

Arriagada PV, Growdon JH, Hedley-Whyte ET, Hyman BT. 1992. Neurofibrillary tangles but not senile plaques parallel duration and severity of Alzheimer's disease. Neurology 42(3 Pt 1):631-639.

Ashburner J, Friston KJ. 1999. Nonlinear spatial normalization using basis functions. Hum Brain Mapp 7(4):254-266.

Augustinack JC, Helmer K, Huber KE, Kakunoori S, Zollei L, Fischl B. 2010. Direct visualization of the perforant pathway in the human brain with ex vivo diffusion tensor imaging. Front Hum Neurosci 4:42.

Augustinack JC, Huber K, Postelnicu GM, Pienaar R, Fischl B. 2012a. Entorhinal verrucae correlate with surface geometry. Translational Neuoscience 3(2):123-131.

Augustinack JC, Huber KE, Postelnicu GM, Kakunoori S, Wang R, van der Kouwe AJ, Wald LL, Stein TD, Frosch MP, Fischl B. 2012b. Entorhinal verrucae geometry is coincident and correlates with Alzheimer's lesions: a combined neuropathology and high-resolution ex vivo MRI analysis. Acta Neuropathol 123(1):85-96.

Augustinack JC, Huber KE, Stevens AA, Roy M, Frosch MP, van der Kouwe AJ, Wald LL, Van Leemput K, McKee AC, Fischl B. 2013. Predicting the location of human perirhinal cortex, Brodmann's area 35, from MRI. Neuroimage 64:32-42.

Augustinack JC, van der Kouwe AJ, Blackwell ML, Salat DH, Wiggins CJ, Frosch MP, Wiggins GC, Potthast A, Wald LL, Fischl BR. 2005. Detection of entorhinal layer II using 7Tesla magnetic resonance imaging. Ann Neurol 57(4):489-494.

Baltes C, Princz-Kranz F, Rudin M, Mueggler T. 2011. Detecting amyloid-beta plaques in Alzheimer's disease. Methods Mol Biol 711:511-533.

Barbier EL, Marrett S, Danek A, Vortmeyer A, van Gelderen P, Duyn J, Bandettini P, Grafman J, Koretsky AP. 2002. Imaging cortical anatomy by high-resolution MR at 3.0T: detection of the stripe of Gennari in visual area 17. Magn Reson Med 48(4):735-738.

Basser PJ. 1994. Focal magnetic stimulation of an axon. IEEE Trans Biomed Eng 41(6):601-606.

Basser PJ, Mattiello J, LeBihan D. 1994. MR diffusion tensor spectroscopy and imaging. Biophys J 66(1):259-267.

Belliveau JW, Rosen BR, Kantor HL, Rzedzian RR, Kennedy DN, McKinstry RC, Vevea JM, Cohen MS, Pykett IL, Brady TJ. 1990. Functional cerebral imaging by susceptibility-contrast NMR. Magn Reson Med 14(3):538-546.

Bennett DA, Schneider JA, Bienias JL, Evans DA, Wilson RS. 2005. Mild cognitive impairment is related to Alzheimer disease pathology and cerebral infarctions. Neurology 64(5):834-841.

Blezer EL, Bauer J, Brok HP, Nicolay K, t Hart BA. 2007. Quantitative MRI-pathology correlations of brain white matter lesions developing in a non-human primate model of multiple sclerosis. NMR Biomed 20(2):90-103.

Braak H, Braak E. 1985. On areas of transition between entorhinal allocortex and temporal isocortex in the human brain. Normal morphology and lamina-specific pathology in Alzheimer's disease. Acta Neuropathol 68(4):325-332.

Braak H, Braak E. 1991. Neuropathological stageing of Alzheimer-related changes. Acta Neuropathol (Berl) 82(4):239-259.

Bridge H, Clare S. 2006. High-resolution MRI: in vivo histology? Philos Trans R Soc Lond B Biol Sci 361(1465):137-146.

Broca P. 1878. Anatomie comparee des circonvolutions cerebrales. Revue D'Anthropologie:385-498.

Brodmann K. 1909. Vergleichende Lokalisationslehre der Groshirnrinde. Leipzig: Verlag von Johann Ambrosius Barth.

Brodmann K. 1994. Brodmann's Localisation in the Cerebral Cortex. translated by Garey L, translator. London: Smith-Gordon

Clark VP, Courchesne E, Grafe M. 1992. In vivo myeloarchitectonic analysis of human striate and extrastriate cortex using magnetic resonance imaging. Cereb Cortex 2(5):417-424.

Connolly CJ. 1950. External Morphology of the Primate Brain. In: Thomas C, editor. Springfield.

Cowin GJ, Butler TJ, Kurniawan ND, Watson C, Wallace RH. 2011. Magnetic resonance microimaging of the spinal cord in the SOD1 mouse model of amyotrophic lateral sclerosis detects motor nerve root degeneration. Neuroimage 58(1):69-74.

De Toledo-Morrell L, Goncharova I, Dickerson B, Wilson RS, Bennett DA. 2000. From healthy aging to early Alzheimer's disease: in vivo detection of entorhinal cortex atrophy. Ann N Y Acad Sci 911:240-253.

Desikan RS, Cabral HJ, Fischl B, Guttmann CR, Blacker D, Hyman BT, Albert MS, Killiany RJ. 2009a. Temporoparietal MR imaging measures of atrophy in subjects with mild cognitive impairment that predict subsequent diagnosis of Alzheimer disease. AJNR Am J Neuroradiol 30(3):532-538.

Desikan RS, Cabral HJ, Hess CP, Dillon WP, Glastonbury CM, Weiner MW, Schmansky NJ, Greve DN, Salat DH, Buckner RL, Fischl B. 2009b. Automated MRI measures identify individuals with mild cognitive impairment and Alzheimer's disease. Brain : a journal of neurology 132(Pt 8):2048-2057.

Desikan RS, Cabral HJ, Settecase F, Hess CP, Dillon WP, Glastonbury CM, Weiner MW, Schmansky NJ, Salat DH, Fischl B. 2010. Automated MRI measures predict progression to Alzheimer's disease. Neurobiol Aging 31(8):1364-1374.

Desikan RS, Fischl B, Cabral HJ, Kemper TL, Guttmann CR, Blacker D, Hyman BT, Albert MS, Killiany RJ. 2008. MRI measures of temporoparietal regions show differential rates of atrophy during prodromal AD. Neurology 71(11):819-825.

deToledo-Morrell L, Stoub TR, Bulgakova M, Wilson RS, Bennett DA, Leurgans S, Wuu J, Turner DA. 2004. MRI-derived entorhinal volume is a good predictor of conversion from MCI to AD. Neurobiol Aging 25(9):1197-1203.

Dickerson BC, Feczko E, Augustinack JC, Pacheco J, Morris JC, Fischl B, Buckner RL. 2009. Differential effects of aging and Alzheimer's disease on medial temporal lobe cortical thickness and surface area. Neurobiol Aging 30(3):432-440.

Dickerson BC, Stoub TR, Shah RC, Sperling RA, Killiany RJ, Albert MS, Hyman BT, Blacker D, Detoledo-Morrell L. 2011. Alzheimer-signature MRI biomarker predicts AD dementia in cognitively normal adults. Neurology 76(16):1395-1402.

Ding SL, Van Hoesen GW. 2010. Borders, extent, and topography of human perirhinal cortex as revealed using multiple modern neuroanatomical and pathological markers. Hum Brain Mapp 31(9):1359-1379.

Ding SL, Van Hoesen GW, Cassell MD, Poremba A. 2009. Parcellation of human temporal polar cortex: a combined analysis of multiple cytoarchitectonic, chemoarchitectonic, and pathological markers. The Journal of comparative neurology 514(6):595-623.

Doyle FH, Gore JC, Pennock JM, Bydder GM, Orr JS, Steiner RE, Young IR, Burl M, Clow H, Gilderdale DJ, Bailes DR, Walters PE. 1981. Imaging of the brain by nuclear magnetic resonance. Lancet 2(8237):53-57.

Duyn JH, van Gelderen P, Li TQ, de Zwart JA, Koretsky AP, Fukunaga M. 2007. High-field MRI of brain cortical substructure based on signal phase. Proc Natl Acad Sci U S A 104(28):11796-11801.

Eickhoff S, Walters NB, Schleicher A, Kril J, Egan GF, Zilles K, Watson JD, Amunts K. 2005. High-resolution MRI reflects myeloarchitecture and cytoarchitecture of human cerebral cortex. Hum Brain Mapp 24(3):206-215.

Eickhoff SB, Heim S, Zilles K, Amunts K. 2006a. Testing anatomically specified hypotheses in functional imaging using cytoarchitectonic maps. Neuroimage 32(2):570-582.

Eickhoff SB, Schleicher A, Zilles K, Amunts K. 2006b. The human parietal operculum. I. Cytoarchitectonic mapping of subdivisions. Cereb Cortex 16(2):254-267.

Fatterpekar GM, Naidich TP, Delman BN, Aguinaldo JG, Gultekin SH, Sherwood CC, Hof PR, Drayer BP, Fayad ZA. 2002. Cytoarchitecture of the human cerebral cortex: MR microscopy of excised specimens at 9.4 Tesla. AJNR Am J Neuroradiol 23(8):1313-1321.

Filimonov IN. 1949. Sravnitel'naya Anatomiya Kory Bol'shogo Mozga, Mlekopitayushchikh Paleokorteks, Arkhukorteks, Mechutochnaya Kora. Academy of Medical Sciences. Moscow. p 1-262.

Fischl B, Salat DH, Busa E, Albert M, Dieterich M, Haselgrove C, van der Kouwe A, Killiany R, Kennedy D, Klaveness S, Montillo A, Makris N, Rosen B, Dale AM. 2002. Whole brain segmentation: automated labeling of neuroanatomical structures in the human brain. Neuron 33(3):341-355.

Fischl B, Salat DH, van der Kouwe AJ, Makris N, Segonne F, Quinn BT, Dale AM. 2004a. Sequence-independent segmentation of magnetic resonance images. Neuroimage 23 Suppl 1:S69-84.

Fischl B, Sereno MI, Dale AM. 1999a. Cortical surface-based analysis. II: Inflation, flattening, and a surface-based coordinate system. Neuroimage 9(2):195-207.

Fischl B, Sereno MI, Tootell RB, Dale AM. 1999b. High-resolution intersubject averaging and a coordinate system for the cortical surface. Hum Brain Mapp 8(4):272-284.

Fischl B, Stevens AA, Rajendran N, Yeo BT, Greve DN, Van Leemput K, Polimeni JR, Kakunoori S, Buckner RL, Pacheco J, Salat DH, Melcher J, Frosch MP, Hyman BT, Grant PE, Rosen BR, van der Kouwe AJ, Wiggins GC, Wald LL, Augustinack JC. 2009. Predicting the location of entorhinal cortex from MRI. Neuroimage 47(1):8-17.

Fischl B, van der Kouwe A, Destrieux C, Halgren E, Segonne F, Salat DH, Busa E, Seidman LJ, Goldstein J, Kennedy D, Caviness V, Makris N, Rosen B, Dale AM. 2004b. Automatically parcellating the human cerebral cortex. Cereb Cortex 14(1):11-22.

Garbelli R, Zucca I, Milesi G, Mastropietro A, D'Incerti L, Tassi L, Colombo N, Marras C, Villani F, Minati L, Spreafico R. 2011. Combined 7-T MRI and histopathologic study of normal and dysplastic samples from patients with TLE. Neurology 76(13):1177-1185.

Geyer S, Weiss M, Reimann K, Lohmann G, Turner R. 2011. Microstructural Parcellation of the Human Cerebral Cortex - From Brodmann's Post-Mortem Map to in vivo Mapping with High-Field Magnetic Resonance Imaging. Front Hum Neurosci 5:19.

Giannakopoulos P, Herrmann FR, Bussiere T, Bouras C, Kovari E, Perl DP, Morrison JH, Gold G, Hof PR. 2003. Tangle and neuron numbers, but not amyloid load, predict cognitive status in Alzheimer's disease. Neurology 60(9):1495-1500.

Gloor P. 1997. The Temporal Lobe and Limbic System. New York: Oxford University Press.

Gomez-Isla T, Hollister R, West H, Mui S, Growdon JH, Petersen RC, Parisi JE, Hyman BT. 1997. Neuronal loss correlates with but exceeds neurofibrillary tangles in Alzheimer's disease. Ann Neurol 41(1):17-24.

Hanke J. 1997. Sulcal pattern of the anterior parahippocampal gyrus in the human adult. Annals of anatomy = Anatomischer Anzeiger : official organ of the Anatomische Gesellschaft 179(4):335-339.

Hof PR, Bussiere T, Gold G, Kovari E, Giannakopoulos P, Bouras C, Perl DP, Morrison JH. 2003. Stereologic evidence for persistence of viable neurons in layer II of the entorhinal cortex and the CA1 field in Alzheimer disease. J Neuropathol Exp Neurol 62(1):55-67.

Howe KL, Dimitri D, Heyn C, Kiehl TR, Mikulis D, Valiante T. 2010. Histologically confirmed hippocampal structural features revealed by 3T MR imaging: potential to increase diagnostic specificity of mesial temporal sclerosis. AJNR Am J Neuroradiol 31(9):1682-1689.

Hyman BT, Van Hoesen GW, Damasio AR, Barnes CL. 1984. Alzheimer's disease: cell-specific pathology isolates the hippocampal formation. Science 225(4667):1168-1170.

Insausti R, Insausti AM, Sobreviela MT, Salinas A, Martinez-Penuela JM. 1998a. Human medial temporal lobe in aging: anatomical basis of memory preservation. Microscopy research and technique 43(1):8-15.

Insausti R, Juottonen K, Soininen H, Insausti AM, Partanen K, Vainio P, Laakso MP, Pitkanen A. 1998b. MR volumetric analysis of the human entorhinal, perirhinal, and temporopolar cortices. AJNR Am J Neuroradiol 19(4):659-671.

Jenkinson M, Beckmann CF, Behrens TE, Woolrich MW, Smith SM. 2012. Fsl. Neuroimage 62(2):782-790.

Kangarlu A, Bourekas EC, Ray-Chaudhury A, Rammohan KW. 2007. Cerebral cortical lesions in multiple sclerosis detected by MR imaging at 8 Tesla. AJNR Am J Neuroradiol 28(2):262-266.

Klingler J. 1948. Die makroskopische Anatomie der Ammonsformation. Denkschr Schweiz Naturforsch 78(82).

Krieg WJS. 1973. Architectonics of Human Cerebral Fiber Systems. Evanston: Brain Books.

Lauterbur PC. 1973. Image formation by induced local interactions. Examples employing nuclear magnetic resonance. . Clin Orthop Relat Res(244):3-6.

Lorente de No R. 1934. Studies on the structure of the cerebral cortex II Continuation of the study of ammonic system. Journal Fur Psychologie and Neurologie 46(6):113-177.

Mansfield P, Grannell PK. 1973. NMR diffraction in solids? J Phys C: Solid State Phys 6:L4226.

Mesulam MM, Mufson EJ. 1982. Insula of the old world monkey. I. Architectonics in the insulo-orbito-temporal component of the paralimbic brain. The Journal of comparative neurology 212(1):1-22.

Nabuurs RJ, Hegeman I, Natte R, van Duinen SG, van Buchem MA, van der Weerd L, Webb AG. 2011. High-field MRI of single histological slices using an inductively coupled, self-resonant microcoil: application to ex vivo samples of patients with Alzheimer's disease. NMR Biomed 24(4):351-357.

Nelson PT, Braak H, Markesbery WR. 2009. Neuropathology and cognitive impairment in Alzheimer disease: a complex but coherent relationship. J Neuropathol Exp Neurol 68(1):1-14.

Netter FH. 1989. Altas of Human Anatomy. Colacino S, editor: Cibs Ciba-Geigy Corporation, Summit.

Ogawa S, Lee TM, Kay AR, Tank DW. 1990. Brain magnetic resonance imaging with contrast dependent on blood oxygenation. Proc Natl Acad Sci U S A 87(24):9868-9872.

Ono M, Kubik, S., Abernathey, C.D. 1990 Atlas of the Cerebral Sulci. New York: Georg Thieme Verlag.

Owen R. 1868. Prosencephalon of Mammals. Anatomy of Vertebrates. London: Longmans, Green & Co. p 98-146.

Pandya DN, Yeterian E. 1985. Architecture and Connections of Cortical Association Areas. In: Peters A, Jones EG, editors. Cerebral Cortex, Association and Auditory Cortices. New York: Plenum Press. p 179-226.

Post MJ. 2008. A new era in neuroradiology: ex vivo validation of in vivo imaging research. AJNR Am J Neuroradiol 29(2):212-213.

Rademacher J, Burgel U, Geyer S, Schormann T, Schleicher A, Freund HJ, Zilles K. 2001. Variability and asymmetry in the human precentral motor system. A cytoarchitectonic and myeloarchitectonic brain mapping study. Brain : a journal of neurology 124(Pt 11):2232-2258.

Retzius G. 1896. Das Menschenhirn. Stockholm: Norstedt and Sonhe.

Reuter M, Sand P, Huber K, Nguyen K, Saygin Z, Rosas HD, Augustinack J, Fischl B. 2012. Registration of Histology and MRI using Blockface as Intermediate Space.

Riddle A, Dean J, Buser JR, Gong X, Maire J, Chen K, Ahmad T, Cai V, Nguyen T, Kroenke CD, Hohimer AR, Back SA. 2011. Histopathological correlates of magnetic resonance imaging-defined chronic perinatal white matter injury. Ann Neurol 70(3):493-507.

Sand P, Teller S. 2008. Particle video: Long-range motion estimation using point trajectories. International Journal of Computer Vision 80(1):72-91.

Sanides F. 1969. Comparative architectonics of the neocortex of mammals and their evolutionary interpretation. Annals of the New York Academy of Sciences 167:404-423.

Savva GM, Wharton SB, Ince PG, Forster G, Matthews FE, Brayne C. 2009. Age, neuropathology, and dementia. N Engl J Med 360(22):2302-2309.

Scheperjans F, Eickhoff SB, Homke L, Mohlberg H, Hermann K, Amunts K, Zilles K. 2008a. Probabilistic maps, morphometry, and variability of cytoarchitectonic areas in the human superior parietal cortex. Cereb Cortex 18(9):2141-2157.

Scheperjans F, Hermann K, Eickhoff SB, Amunts K, Schleicher A, Zilles K. 2008b. Observer-independent cytoarchitectonic mapping of the human superior parietal cortex. Cereb Cortex 18(4):846-867.

Scoville WB, Milner B. 1957. Loss of recent memory after bilateral hippocampal lesions. J Neurol Neurosurg Psychiatry 20(1):11-21.

Shepherd TM, Ozarslan E, Yachnis AT, King MA, Blackband SJ. 2007. Diffusion tensor microscopy indicates the cytoarchitectural basis for diffusion anisotropy in the human hippocampus. AJNR Am J Neuroradiol 28(5):958-964.

Simic G, Bexheti S, Kelovic Z, Kos M, Grbic K, Hof PR, Kostovic I. 2005. Hemispheric asymmetry, modular variability and age-related changes in the human entorhinal cortex. Neuroscience 130(4):911-925.

Smith GE. 1903. On the so-called 'gyri hippocampi'. Journal of Anatomy and Physiology XXXVII:324-328.

Smith SM, Jenkinson M, Woolrich MW, Beckmann CF, Behrens TE, Johansen-Berg H, Bannister PR, De Luca M, Drobnjak I, Flitney DE, Niazy RK, Saunders J, Vickers J, Zhang Y, De Stefano N, Brady JM, Matthews PM. 2004. Advances in functional and structural MR image analysis and implementation as FSL. Neuroimage 23 Suppl 1:S208-219.

Solodkin A, Van Hoesen GW. 1996. Entorhinal cortex modules of the human brain. The Journal of comparative neurology 365(4):610-617.

Stephan H. 1975. In Handbuch der mikroskopischen Anatomie des Menschen. Bargmann W, editor. Berlin and New York.: Springer-Verlag. 998 p.

Turner W. 1890. The convolutions of the brain: a study in comparative anatomy. Journal of Anatomy and Physiology of Normal and Pathological 25:105-153.

Van Hoesen G, Pandya DN. 1975a. Some connections of the entorhinal (area 28) and perirhinal (area 35) cortices of the rhesus monkey. I. Temporal lobe afferents. Brain Res 95(1):1-24.

Van Hoesen GW. 1982. The parahippocampal gyrus: new observations regarding its cortical connections in the monkey. Trends in Neuroscience 5:345-350.

Van Hoesen GW, Augustinack JC, Dierking J, Redman SJ, Thangavel R. 2000. The parahippocampal gyrus in Alzheimer's disease. Clinical and preclinical neuroanatomical correlates. Ann N Y Acad Sci 911:254-274.

Van Hoesen GW, Pandya DN. 1975b. Some connections of the entorhinal (area 28) and perirhinal (area 35) cortices of the rhesus monkey. III. Efferent connections. Brain Res 95(1):39-59.

Van Hoesen GW, Pandya DN, Butters N. 1972. Cortical afferents to the entorhinal cortex of the Rhesus monkey. Science 175(4029):1471-1473.

Van Hoesen GW, Solodkin A. 1993. Some modular features of temporal cortex in humans as revealed by pathological changes in Alzheimer's disease. Cereb Cortex 3(5):465-475.

Wachinger C. 2010. Structural image representation for image registration. Proceedings of IEEE Computer Vision and Pettern Recognition Workshops:23-30. .

Walters NB, Egan GF, Kril JJ, Kean M, Waley P, Jenkinson M, Watson JD. 2003. In vivo identification of human cortical areas using high-resolution MRI: an approach to cerebral structure-function correlation. Proc Natl Acad Sci U S A 100(5):2981-2986.

Yassa MA, Muftuler LT, Stark CE. 2010. Ultrahigh-resolution microstructural diffusion tensor imaging reveals perforant path degradation in aged humans in vivo. Proc Natl Acad Sci U S A 107(28):12687-12691.

Zeineh MM, Holdsworth S, Skare S, Atlas SW, Bammer R. 2012. Ultra-high resolution diffusion tensor imaging of the microscopic pathways of the medial temporal lobe. Neuroimage 62(3):2065-2082.

Zilles K, Amunts K. 2009. Receptor mapping: architecture of the human cerebral cortex. Curr Opin Neurol 22(4):331-339.

Zuckerkandl E, editor. 1887. Uber Das Riechcentrum Eine Vergleichend-Anatomische Studie. Stuttgart: Verlag Von Ferdinand Enke.

ABBREVIATIONS

ab = angular bundle
alv = alveus
AM = Amygdala
AD = Alzheimer's disease
BA = Brodmann's area
CA = cornu ammonis
CP = choroid plexsus
CS = collateral sulcus
DG = dentate gyrus
EC = entorhinal cortex
FLASH = fast low angle shot
HF = hippocampal fissure
HP = hippocampus
iso = isocortex
mf = mossy fiber
ml = molecular layer
MRI = magnetic resonance imaging
OTS = occipital temporal sulcus
PC = perirhinal cortex
pp = perforant pathway
ParaS = parasubiculum
PreS = presubiculum
Pyr = pyramidal layer
RG = rhinal groove
RS = rhinal sulcus
SUB = subiculum
SNR = signal to noise ratio
TP = temporal pole

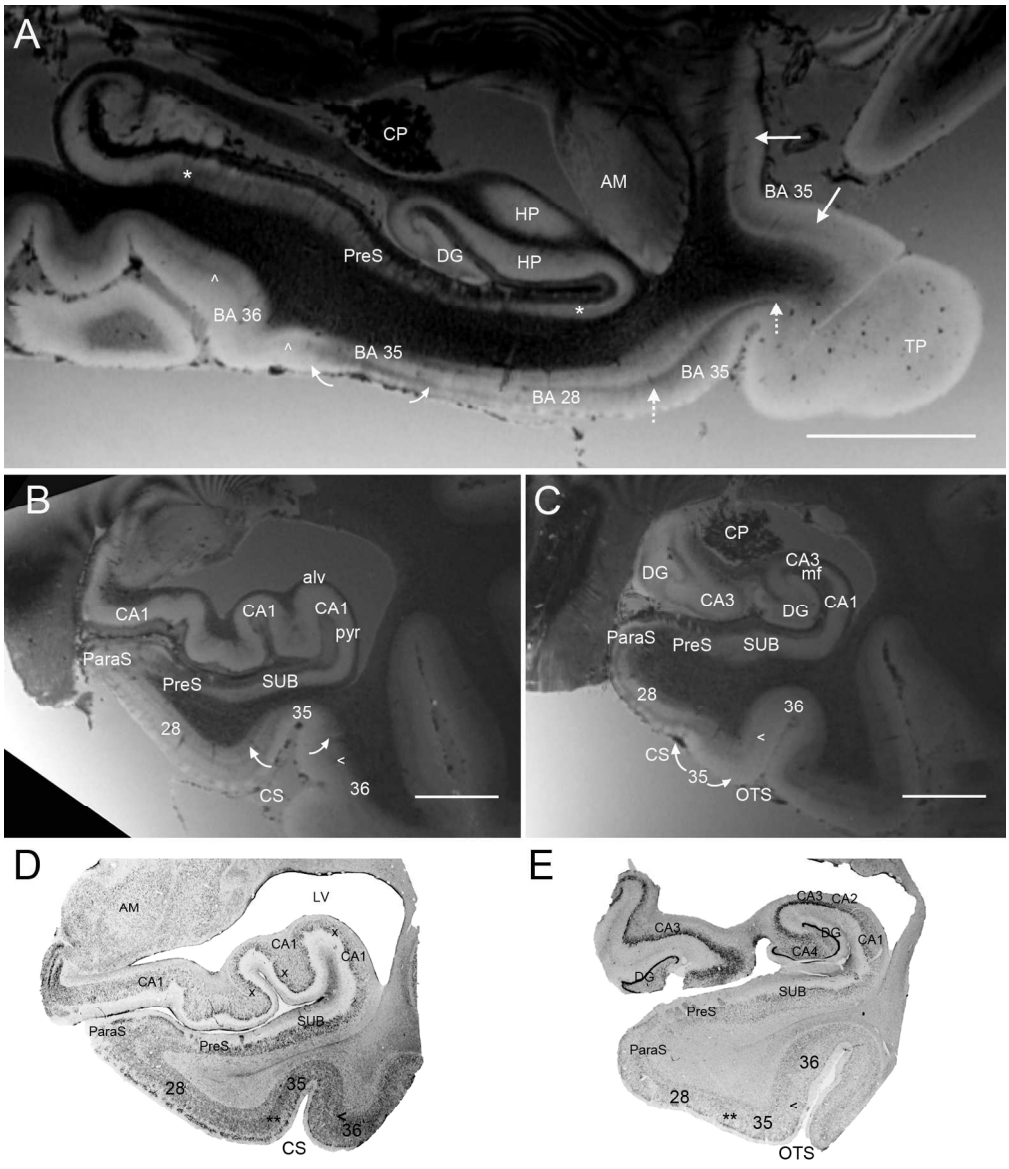

158x189mm (300 x 300 DPI)

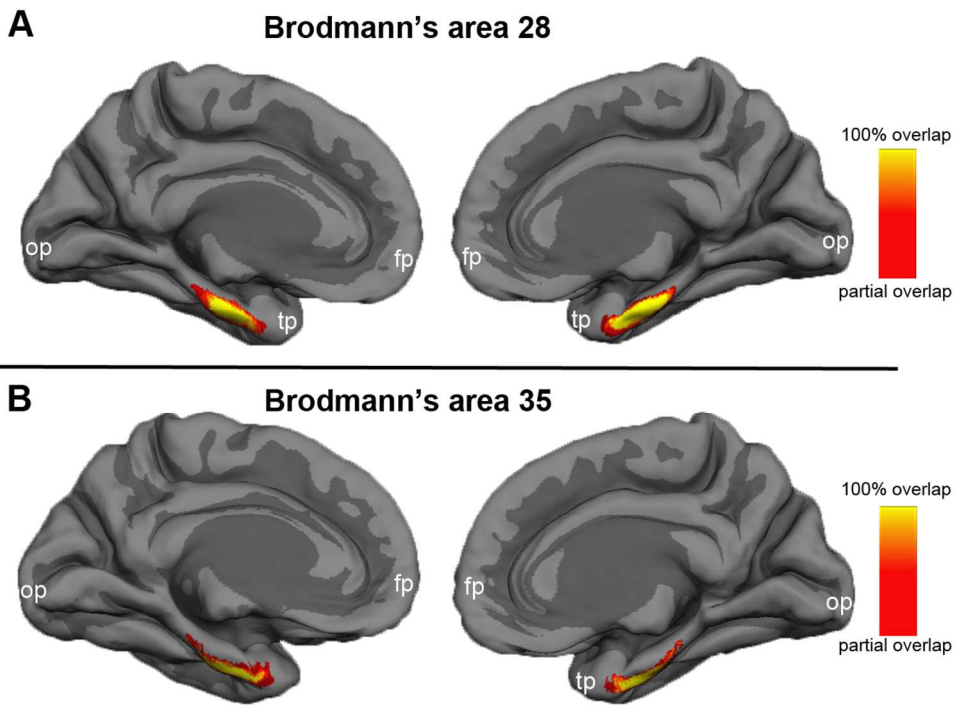

117x83mm (300 x 300 DPI)

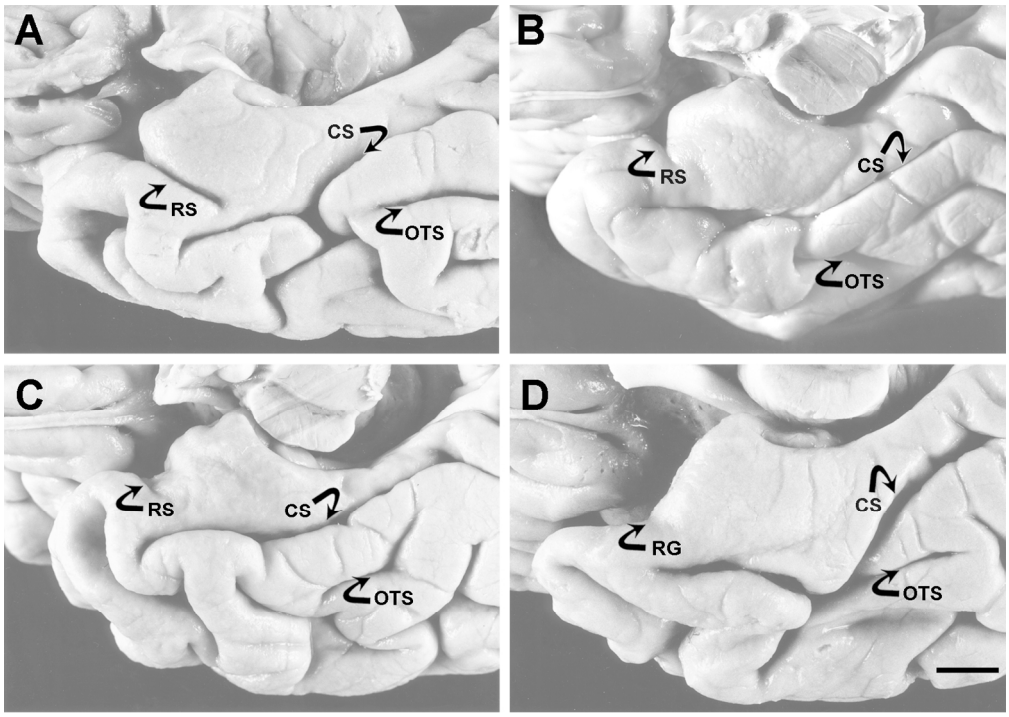

143x101mm (300 x 300 DPI)

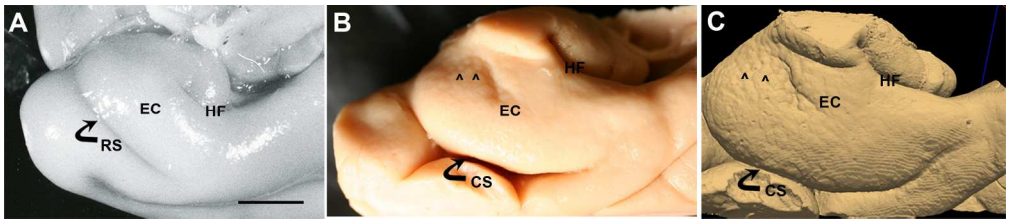

177x37mm (300 x 300 DPI)

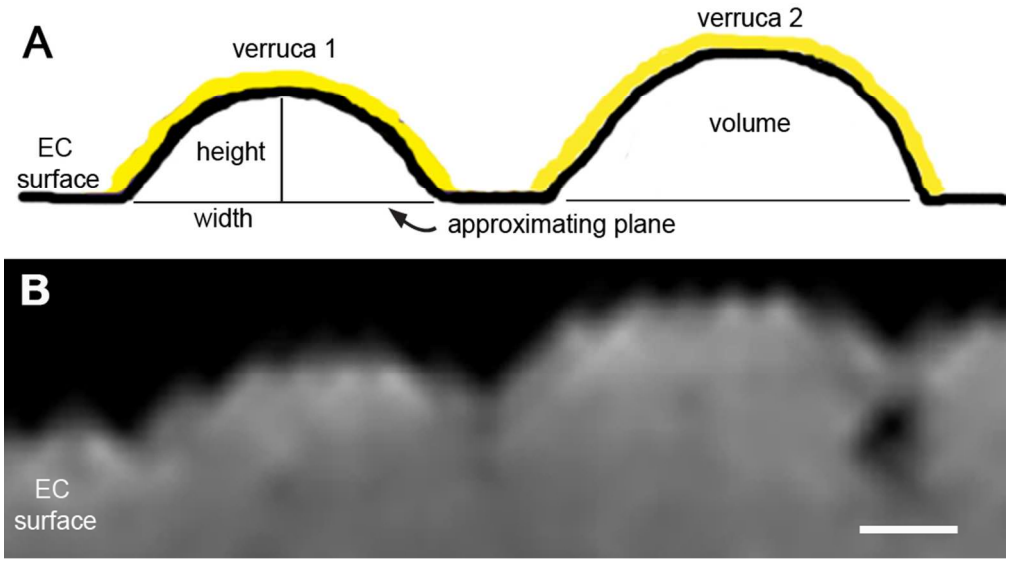

89x49mm (300 x 300 DPI)

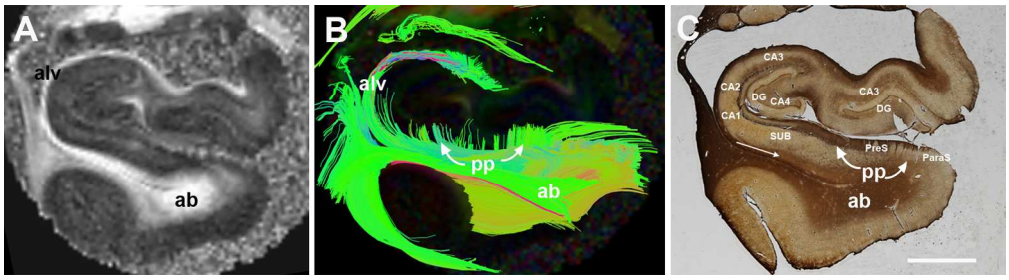

177x47mm (300 x 300 DPI)

Using *ex vivo* MRI combined with a histological paradigm, the authors show that Nissl and myelin stained tissue validates ultra-high resolution MRI and this approach links the histological ground truth and *in vivo* brain modeling. *Ex vivo* MRI optimally models small structures involved in Alzheimer's disease.

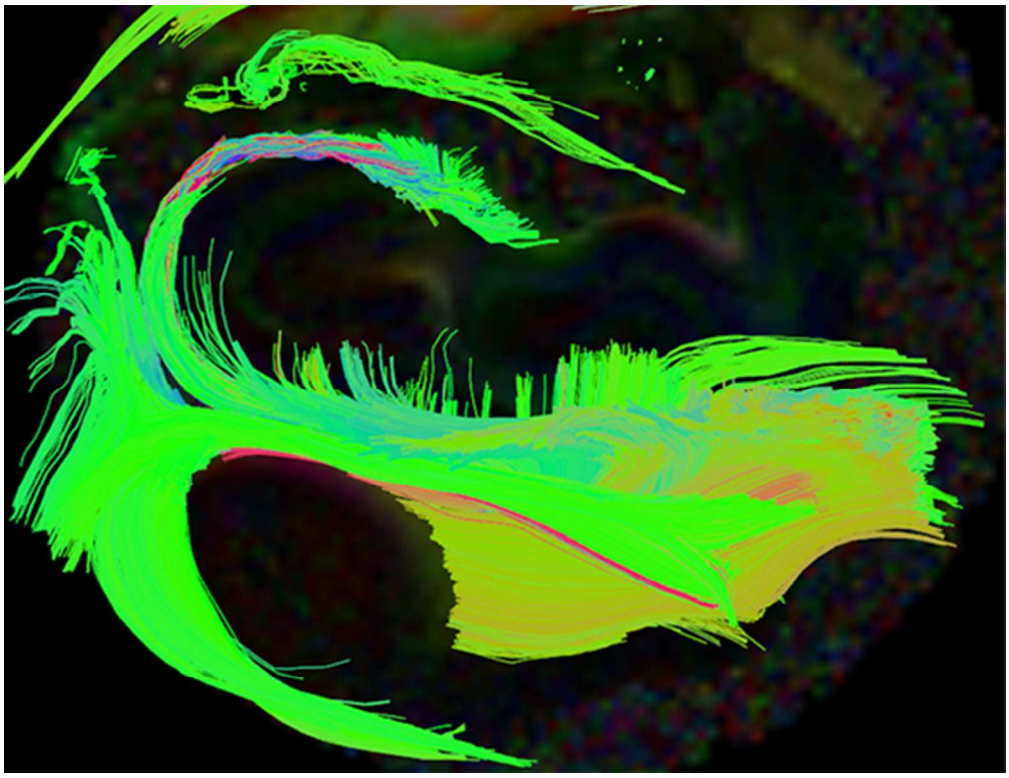

62x47mm (300 x 300 DPI)